Plastic deformation of bulk and micropillar single crystals of Mo_5Si_3 with the tetragonal $D8_m$ structure

Kyosuke Kishida [a,b,*], Zhenghao Chen [a,b], Hirotaka Matsunoshita [a], Takuto Maruyama [a], Takayoshi Fukuyama [a], Yuta Sasai [a], Haruyuki Inui [a,b], Martin Heilmaier [c]

[a] Department of Materials Science and Engineering, Kyoto University, Sakyo-ku, Kyoto 606-8501, Japan
[b] Center for Elements Strategy Initiative for Structural Materials (ESISM), Kyoto University, Sakyo-ku, Kyoto 606-8501, Japan
[c] Institute for Applied Materials (IAM-WK), Karlsruhe Institute of Technology (KIT), Engelbert-Arnold-Strasse 4, Karlsruhe 76131, Germany

ARTICLE INFO

ABSTRACT

The plastic deformation behavior of single crystals of Mo_5Si_3 with the tetragonal $D8_m$ structure has been investigated in compression as a function of crystal orientation and temperature (1200–1500°C) in the bulk form and as a function of crystal orientation and specimen size at room temperature in the micropillar form. The slip system of $\{11\overline{2}\}{<}111{>}$ is identified to be the only one that operates at high temperatures above 1200°C in bulk crystals, while any plastic flow is not detected at room temperature in micropillar crystals. The critical resolved shear stress (CRSS) for $\{11\overline{2}\}{<}111{>}$ slip at room temperature estimated from the extrapolation of the temperature dependence of CRSS obtained for bulk crystals is considerably higher than fracture stresses obtained for micropillar crystals, indicating that the room-temperature brittleness is due in principle to the difficulty in dislocation motion arising from the very high CRSS value. The value of fracture toughness evaluated with a chevron-notched micro-beam specimen with a notch plane parallel to (001) is 1.54 MPa•m$^{1/2}$, which is comparable to those reported for other transition-metal (TM) silicides of the TM_5Si_3-type. The selection of $\{11\overline{2}\}$ slip plane and the dissociation of the $1/2{<}111{>}$ dislocation on the slip plane are discussed based on generalized stacking fault energy (GSFE) curves theoretically calculated by first-principles calculations.

1. Introduction

There is an ever-increasing demand for ultra high-temperature materials that can withstand severe environments such as very high turbine inlet temperatures around 1600 °C of the most advanced gas turbine combustion systems (Jackson et al., 1996; Perepezko, 2009; Zhao and Westbrook, 2003). This is because significant reduction of climate-warming CO_2 emission is expected with the improved thermal efficiency of combustion systems in fossil-fueled power plants by drastically raising their operating temperature. In view of this, transition-metal (TM) silicides of the $TMSi_2$- and TM_5Si_3-types are particularly of interest, because many of them possess the melting temperature higher than 2000 °C and exhibit excellent oxidation resistance because of their high Si contents (Akinc et al., 1999; Bewley et al., 2003; Ito et al., 1997; Kishida et al., 2010; Mitra, 2006, 2015; Petrovic and Vasudevan, 1999; Tsakiropoulos, 2018,

---

* Corresponding author at: Department of Materials Science and Engineering, Kyoto University, Sakyo-ku, Kyoto 606-8501, Japan.
  E-mail address: kishida.kyosuke.6w@kyoto-u.ac.jp (K. Kishida).

2022; Yamaguchi et al., 2000). While the early studies in 1990s focused on TM silicides of the TMSi$_2$-type, especially on MoSi$_2$ (Inui et al., 2000a, 2000b; Ito et al., 1995, 1997; Maloy et al., 1995; Petrovic and Vasudevan, 1999; Yamaguchi et al., 2000), alloys containing TM silicides of the TM$_5$Si$_3$-type then gradually took place of the subject of extensive study, as multiphase composites between them and a body-centered cubic (BCC) phase might yield increased ductility and toughness at ambient temperature (Akinc et al., 1999; Bewlay et al., 2003; Mitra, 2006, 2015; Perepezko et al., 2021; Tsakiropoulos, 2018, 2022). TM silicides of the TM$_5$Si$_3$-type have the highest melting temperature in many TM-Si binary phase diagrams and they are usually classified into three types depending on the crystal structure; tetragonal D8$_m$, tetragonal D8$_l$, and hexagonal D8$_8$ structures (Villars and Calvert, 1985). TM silicides of the TM$_5$Si$_3$-type formed with TM=Mo, Nb and Ti are representative, respectively, for these three structures. Specially, alloys based on Nb$_5$Si$_3$ and Mo$_5$SiB$_2$ with the D8$_l$ structure have most intensively been studied as reinforcement of a ductile phase in the form of Nb$_{ss}$/Nb$_5$Si$_3$ (ss: solid-solution) and Mo$_{ss}$/ Mo$_5$SiB$_2$ composites (Bewlay et al., 2003; Mitra, 2006, 2015; Perepezko, 2009; Perepezko et al., 2021; Tsakiropoulos, 2018, 2022). Alloys based on Mo$_5$Si$_3$ with the D8$_m$ structure, on the other hand, have been studied in the form of Mo$_{ss}$/Mo$_5$Si$_3$, MoSi$_2$/Mo$_5$Si$_3$ and Mo$_5$Si$_3$/Al$_2$O$_3$ composites (Akinc et al., 1999; Chen et al., 2014; Fujiwara et al., 2014; Jackson et al., 1996; Mason and Van Aken, 1995; Matsunoshita et al., 2016; Obert et al., 2020, 2021; Vega Farje et al., 2019; Yeh and Peng, 2017; Yuge, 2017; Zhu et al., 2020, 2021).

Mo$_5$Si$_3$ has a complex body-centered tetragonal structure called the W$_5$Si$_3$-type structure (the D8$_m$ structure in the Strukturbericht symbol and tI32 in the Pearson's symbol) with the space group of I4/mcm. ($a = 0.9650$ nm, $c = 0.4911$ nm, Christensen, 1983) (Fig. 1 (a)). In the crystal structure, there is no close-packed plane on which dislocations are expected to move easily unlike in simple metals such as face-centered cubic (FCC) and BCC structures. But, some reasonably close-packed planes can be found such as those on (001) at $z = 0$ and 1/2, while those at $z = 1/4$ and 3/4 are obviously less densely packed (Fig. 1(b)). The (001) atomic planes at $z = 0$ and 1/2 are actually related with each other by 180°-rotation about the a-axis, so that they are designated as A and A' atomic planes, respectively. Then, with the atomic plane designated as B at $z = 1/4$ and 3/4, the crystal structure can be described as being made up of these atomic planes stacked in the ABA'B sequence along the c-axis. The crystal structure is also characterized by two distinct atomic chains extending along the c-axis, as shown in Fig. 1. They are linear chains formed with Mo(2) atoms in the 4b site located at (0, 1/2, 1/4) and those formed with Si(2) atoms in the 4a site located at (0, 0, 1/4), the former of which are believed to play a decisive role in determining many physical properties of Mo$_5$Si$_3$ such as thermal and elastic properties (Chu et al., 1999a, 1999b; Rawn et al., 2005; Dharmawardhana et al., 2015; Azim et al., 2017). Since the distance (0.246 nm) between Mo atoms in the linear chain along the c-axis is shorter than that (0.272 nm) in elemental Mo, the short interatomic distance between Mo atoms in the c-axis chains is pointed out to cause significant thermal expansion anisotropy (the thermal expansion coefficient along the c-axis is more than twice that along the a-axis) leading to microcracking during solidification (Chu et al., 1999a, 1999b; Rawn et al., 2005; Dharmawardhana et al., 2015; Azim et al., 2017). The lowest values of shear modulus on (001) are also interpreted along the same line (Chu et al., 1999b). In contrast to deep knowledge extensively accumulated in the thermal and elastic properties, the plastic deformation behavior of Mo$_5$Si$_3$ has understood less deeply. In particular, there seems no general agreement even on the operative slip systems yet. Mason and Van Aken (1995) were the first to conduct deformation experiments on Mo$_5$Si$_3$. They predicted (001)<110>, {100}<010> and {110}[001] as the operative slip systems from the crystal structure (slip plane distance and Burgers vector length) view point and experimentally identified (001)<110> slip (Mason and Van Aken, 1995) and subsequently (001)<100> slip (Meyer et al., 1996) by transmission electron microscopy (TEM) in [314]-oriented single crystals of Mo$_5$Si$_3$ crept at 1400°C. Then, Chu et al. made another prediction from the orientation dependence of shear modulus that {100}[001] and {110}[001] are the possible operative slip systems (Chu et al., 1999b). Yoshimi et al. (2002) subsequently reported from their high-temperature compression tests on Mo$_5$Si$_3$ single crystals that (i) plastic flow is limited to occur only above 1250~1300°C for most orientations and (ii) while (001)<110> is operative for the [111]-oriented crystal (as conformed by TEM), complicated combinations of (001), {100} and {110} slip contribute to deformation of [100] and [101]-oriented crystals from slip trace observations. Recently, Ochiai et al. investigated the compression deformation behavior of single crystals of Cr$_5$Si$_3$ that is isostructural with Mo$_5$Si$_3$ and reported the operation {100}[001] slip for [012]-oriented crystals from slip trace and TEM observations (Ochiai et al., 2011). More recently, Matsunoshita et al. identified the operation of {11$\bar{2}$}<111> slip from slip trace and TEM observations in a [001]-oriented Mo$_5$Si$_3$ grain in a directionally-solidified MoSi$_2$/Mo$_5$Si$_3$ eutectic composite deformed at 1000°C (Matsunoshita et al., 2016). The operation of this {11$\bar{2}$}<111> slip was predicted neither by Mason and Van Aken (1995) and Chu et al. (1999b). All these results indicate that more work is definitely needed to identify the operative slip systems in Mo$_5$Si$_3$ unambiguously with the use of new techniques that were not employed in these previous studies.

The difficulty in identification of the operative slip systems arises obviously from the fact that very high temperatures exceeding
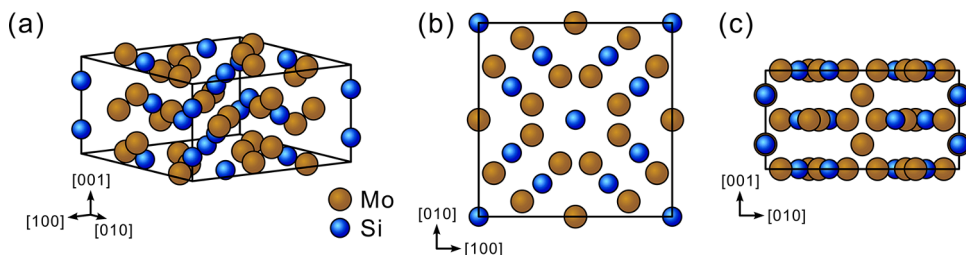

Fig. 1. Crystal structure of Mo$_5$Si$_3$; (a) three-dimensional view, (b) [001] projection and (c) [100] projection.

1250~1300°C are usually needed for plastic flow to occur in single crystals of Mo_5Si_3. At such high temperatures, surface oxide formation is promoted and dislocation climb occurs, respectively making optical slip trace and TEM slip plane determinations difficult. Recent progress in scanning electron microscopy (SEM) has, however, made it ubiquitous to observe dislocations by electron channeling contrast (ECC) imaging (Gutierrez-Urrutia et al., 2009; Han and Crimp, 2020; Picard et al., 2014; Simkin and Crimp, 1999; Weidner and Biermann, 2015; Wilkinson and Hirsch, 1997; Zaefferer and Elhami, 2014). This has opened up a way to identify operative slip systems in brittle materials even if their surface is covered with oxide extensively by high-temperature deformation. Traces of dislocation motion could be detected in the form of 'trains' of dislocations by ECC imaging after polishing out the surface oxide and then crystallographic analysis of the traces can be made together with information from electron backscattered diffraction (EBSD) in the SEM to identify the operative slip systems. In addition, we have successfully demonstrated that micropillar compression at room temperature is very powerful to identify the operative slip systems and their critical resolved shear stress (CRSS) values in various materials including hard and brittle materials such as 6H-SiC and transition-metal (TM) silicides of the $TMSi_2$- and TM_5Si_3-types and so on (Chen et al., 2021; Hashizume et al., 2020, 2021; Higashi et al., 2018; Kishida et al., 2018, 2020a, 2020b, c, 2022a, 2022b; Okamoto et al., 2014). The slip systems thus identified by room-temperature micropillar compression tests are proved to be identical with those identified in the corresponding bulk crystals in most cases (Hashizume et al., 2020, 2021; Higashi et al., 2018; Kishida et al., 2018, 2020a, 2020b, 2022a; Okamoto et al., 2014), although there are some exceptions (Chen et al., 2021; Kishida et al., 2018, 2020c, 2022a).

In the present study, we investigate the plastic deformation behavior of single crystals of Mo_5Si_3 in compression as a function of crystal orientation and temperature (1200–1500°C) in bulk compression and as a function of crystal orientation and specimen size at room temperature in micropillar compression. The main purpose of the present study is to apply SEM-ECC imaging and micropillar compression techniques to identify the operative slip systems in Mo_5Si_3 unambiguously, thus clarifying the existing discrepancies in literature.

2. Experimental procedure

Rod ingots were prepared by Ar arc-melting of high-purity Mo and Si in the stoichiometric composition (Mo-37.5 at.%Si). Single crystals of Mo_5Si_3 were grown from the rod ingots with an optical floating-zone furnace at a growth rate of 10 mm h^{-1} under Ar gas flow. After determining the crystallographic orientations by the X-ray back reflection Laue method, oriented specimens for bulk compression tests with dimensions of $2 \times 2 \times 5$ mm^3 as well as micropillar compression tests were sectioned from the as-grown single crystals by spark-machining. The compression-axis orientations selected were [001], [$\bar{1}$10], [010] and [012], and the highest Schmid factors for some possible deformation modes previously reported are listed in Table 1 for each orientation. All specimens for bulk compression tests were mechanically polished and then finished with 0.3 μm alumina abrasive powders prior to compression tests. Micropillar specimens with a square cross-section having an edge length L ranging from 0.7 to 5 μm and an aspect ratio of approximately 1:2~1:3 were fabricated with a JEOL JIB-4000 focused ion beam (FIB) machine at an operating voltage of 30 kV. Compression tests for bulk specimens were carried out on an Instron-type testing machine at a strain rate of 1×10^{-4} s^{-1} at temperatures ranging from 1200 to 1500°C in vacuum. Micropillar compression tests were conducted at room temperature at a nominal strain rate of 1×10^{-4} s^{-1} with an Agilent Technologies Nano Indenter G200 nanomechanical tester equipped with a flat punch indenter tip under displacement-rate-controlled mode. Deformation structures were examined by optical microscopy (OM), SEM equipped with a field-emission gun (JEOL JSM-7001FA operated at 30 kV) and TEM (JEOL JEM-2100F operated at 200 kV).

Fracture toughness was evaluated by single-cantilever bend testing on chevron-notched micro-beam specimens (l: 12 μm, W: 4.5 μm, B: 3 μm, notch lengths a_0 and a_1, and a crack length a; see the inset of Fig. 9) at room temperature and at a constant displacement rate of 5 nm s^{-1}, as described in our previous paper (Kishida et al., 2018, 2020a, 2020b). The fracture toughness value, K_{IC} was evaluated from the maximum load (P_{max}) with numerical analysis using the following equations proposed by Deng et al. (2010).

Table 1
The highest Schmid factor values for possible deformation mode in Mo_5Si_3 single crystals with four different loading axis orientations. b and d denote the magnitude of slip vector and interplanar spacing, respectively.

Deformation mode	Loading axis orientation				b (nm)	d (nm)	d/b
	[001]	[$\bar{1}$10]	[010]	[012]			
{100}[001]	0	0	0	0	0.491	0.964	1.964
{110}[001]	0	0	0	0.353	0.491	0.682	1.389
{1$\bar{1}$0}<111>	0	0	0.470	0.351	0.725	0.682	0.941
{0$\bar{1}$1}<111>	0.302	0.302	0.302	0.450	0.725	0.438	0.604
{$\bar{2}$11}<111>	0.224	0.224	0.447	0.500	0.725	0.324	0.447
{11$\bar{2}$}<111>	0.319	0.319	0.159	0.356	0.725	0.231	0.319
(001)<100>	0	0	0	0.500	0.964	0.491	0.509
{010}<100>	0	0.5	0	0	0.964	0.964	1.000
{011}<100>	0	0.227	0	0.445	0.964	0.438	0.454
{100}<011>	0	0.446	0	0.227	1.082	0.964	0.891
{0$\bar{1}$1}<011>	0.404	0.202	0.404	0.301	1.082	0.438	0.404

$$K_{IC} = \frac{P_{max}}{B\sqrt{W}} Y_C(\alpha_0, \alpha_1) \tag{1}$$

and

$$Y_C(\alpha_0, \alpha_1) = \sqrt{\frac{1}{2} \frac{dC_V(\alpha)}{d\alpha} \frac{\alpha_1 - \alpha_0}{\alpha - \alpha_0}}\bigg|_{\alpha = \alpha_C} \tag{2}$$

where $Y_C(\alpha_0, \alpha_1)$ is the dimensionless geometrical factor, $C_V(\alpha)$ is compliance of the specimen, $\alpha_0 = a_0/W$, $\alpha_1 = a_1/W$, $\alpha = a/W$, $\alpha_C = a_C/W$, and a_C is a critical crack length (Deng et al., 2010; Mueller et al., 2015).

Generalized stacking fault energy (GSFE) for the $(11\bar{2})$ glide planes were calculated by first-principles DFT using the Vienna ab-initio simulation package (VASP) code (Kresse and Furthmüller, 1996; Vitek and Paidar, 2008). The generalized gradient approximation of Perdew-Burke-Ernzerhof (GGA-PBE) was used to treat the exchange-correlation functional (Perdew et al., 1996). The optimized lattice constants for the standard unit cell calculated with an energy cutoff of 440 eV and Monkhorst-Pack k-point mesh of 6 × 6 × 12 were $a = 0.9679$ nm and $c = 0.4915$ nm, which are in good agreement with the experimental values (Ito et al., 1997). For the GSE and surface energy calculations for the $(11\bar{2})$ planes, supercells each containing 144 atoms with the in-plane units defined by 1/2 [111] and $[1\bar{1}0]$ were used. The height of the supercells was fixed to 3.5836 nm including a vacuum layer of 1.5 nm in thickness. An energy cutoff was set to be 440 eV and Monkhorst-Pack k-point mesh of 8 × 4 × 1 was used (Monkhorst and Pack, 1976). All atoms were relaxed along the direction perpendicular to the glide plane so as to minimize the energy of the supercell with a given in-plane displacement.

3. Results

3.1. Bulk single crystals

3.1.1. Stress-strain behavior and temperature dependence of yield stress

Typical stress strain curves obtained in compression at various temperatures for bulk single crystals with [001], $[\bar{1}10]$, [010] and [012] orientations are shown in Fig. 2. The symbol × in the figure indicates the occurrence of failure. For all orientations, plastic flow is only observed at very high temperatures above 1300℃ (for the [001], $[\bar{1}10]$ and [010] orientations) and above 1200℃ (for the [012] orientation). This is consistent with the results reported for Mo_5Si_3 single crystals by Yoshimi et al. (2002). Below these temperatures, premature failure occurs in the elastic region accompanied by vertical cracking of the cleavage-type, typical of brittle failure. Above these temperatures, the yield stress decreases and the amount of achievable plastic strain increases with increasing temperature so that more than a several % plastic strain can be achieved without failure at 1500℃, regardless of crystal orientation. These results are essentially similar to what is observed for Cr_5Si_3, which is isostructural with Mo_5Si_3, although the onset temperatures for plastic flow are much lower in Cr_5Si_3 (Ochiai et al., 2011).

Fig. 3 shows the temperature dependence of yield stress for the four different orientations investigated. The values of yield stress for these four orientations all decrease monotonously with increasing temperature, as similarly observed in Cr_5Si_3 (Ochiai et al., 2011).

3.1.2. Slip trace and dislocation structure observations

Deformation microstructures of a [001]-oriented single crystal deformed at 1300℃ are shown in Fig. 4. Although the deformation temperature of 1300℃ is the lowest temperature above which plastic deformation occurs for the [001] orientation, the specimen surfaces are extensively covered with oxide scales (Fig. 4(a)) and determination of slip planes through slip trace analysis by optical microscopy is very difficult to make on the (100) and (010) side faces (Fig. 4(b) and (c)). However, ECC imaging after removing surface oxide scales by mechanical polishing clearly reveals dislocations lying on distinct slip planes in the form of 'trains' on these side faces
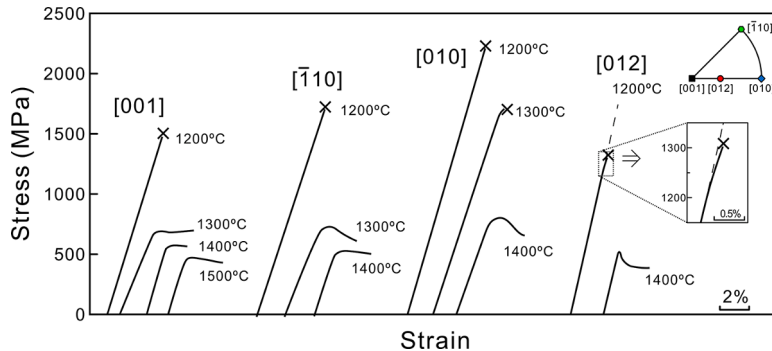

Fig. 2. Typical stress-strain curves obtained in compression for bulk single crystals of Mo_5Si_3 with [001], $[\bar{1}10]$, [100] and [012] orientations. The deformation temperatures are indicated for each of the stress-strain curves. Symbols × indicate the occurrence of failure.
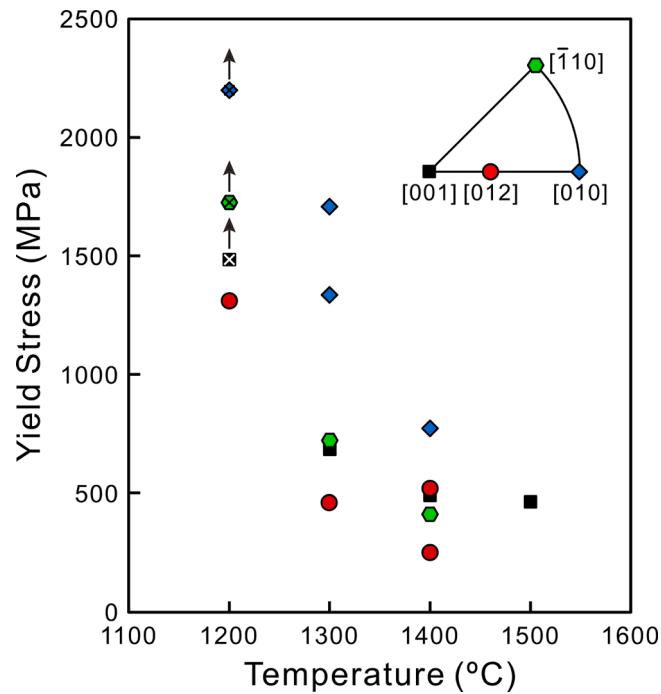
Fig. 3. Temperature dependence of yield stress obtained in compression for bulk single crystals of Mo_5Si_3 with four different orientations. Symbols × indicate stresses at which failure occurred. Arrows are attached to the symbols with × so as to indicate that actual yield stress values are expected to be higher than the plotted ones.
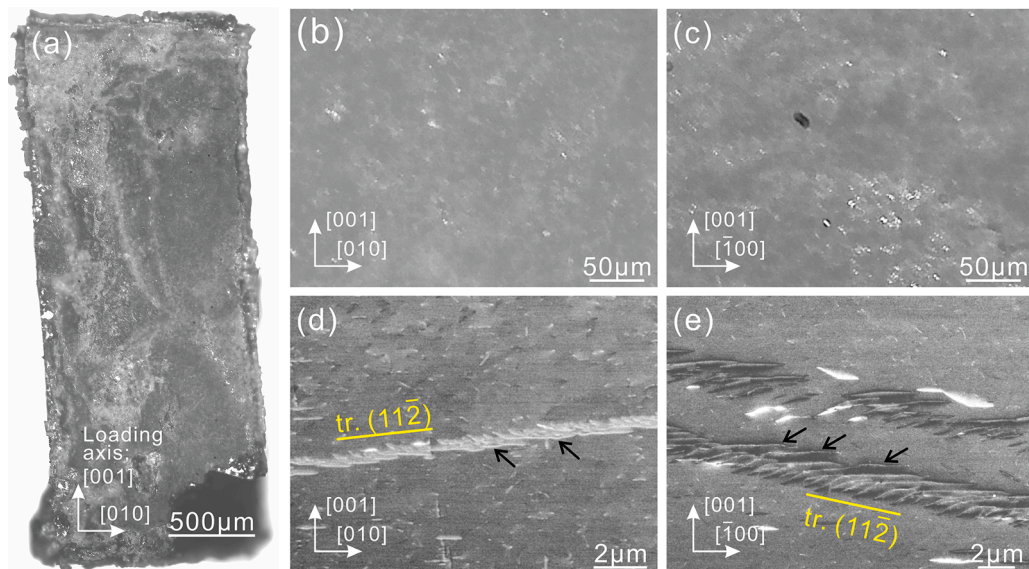

Fig. 4. Deformation microstructures of a [001]-oriented single crystal deformed at 1300C. (a) Appearance of the deformed specimen, (b),(c) optical and (d),(e) ECCI microstructures on (b),(d) (100) and (c),(e) (010) side surfaces.

(Fig. 4(d) and (e)), from which slip trace analysis to determine the slip planes can be successfully made. Although some dislocations are observed to climb out of their original slip planes (indicated by arrows in Fig. 4(d) and (e)), most dislocations are observed in bands with traces parallel to the $(11\bar{2})$ planes on both the (100) and (010) side surfaces. The slip plane that is activated for the [001] orientation is thus determined to be $(11\bar{2})$ for the [001] orientation.

Since specimen surfaces are covered extensively with oxide scales after deformation also for the other three orientations, ECC imaging was utilized to determine the activated slip planes through trace analysis of dislocation trains, as shown in Fig. 5 for (a),(b)
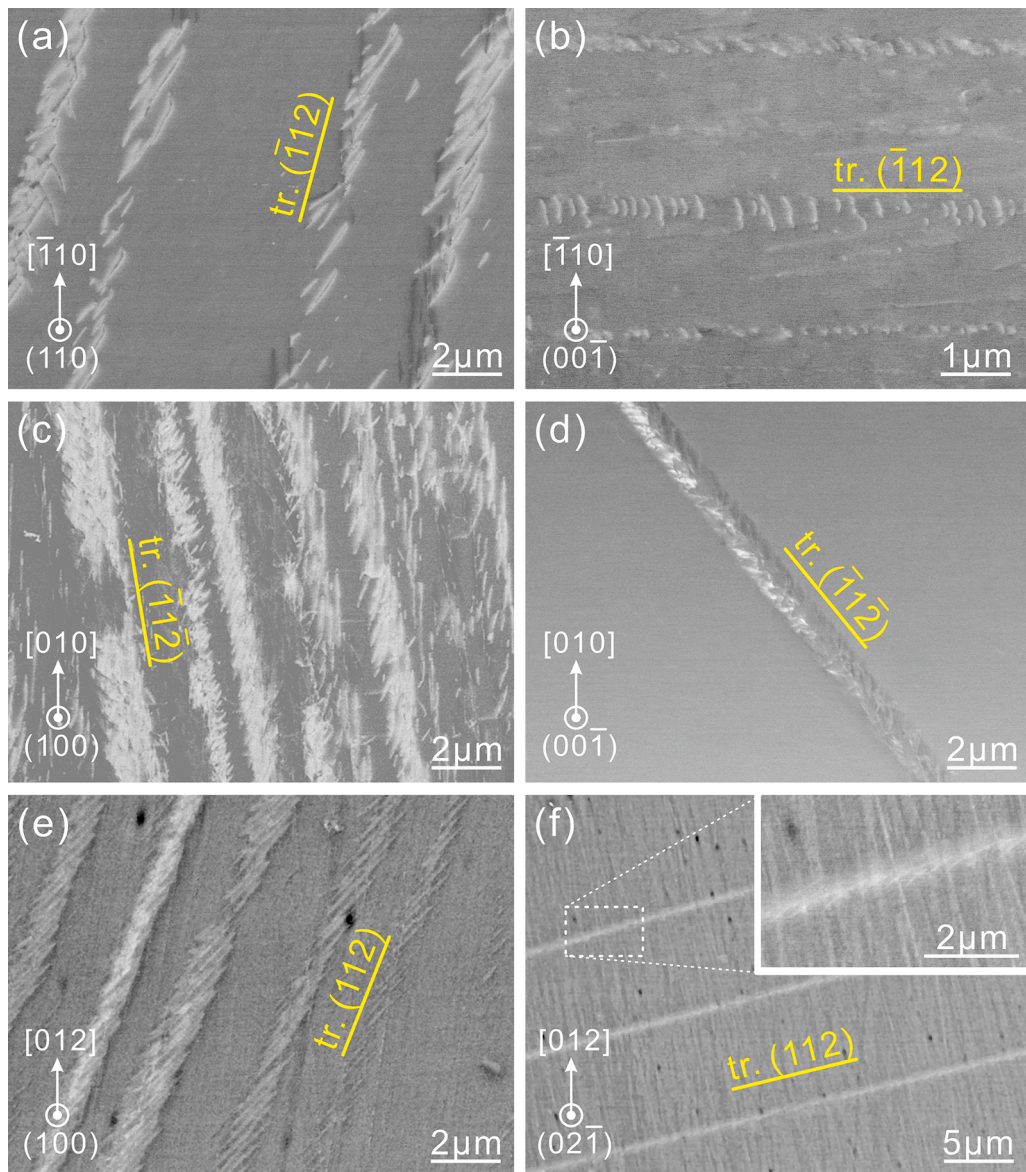
Fig. 5. ECCI microstructures on two side faces of specimens with (a),(b) [$\bar{1}$10], (c),(d) [010] and (e),(f) [012] orientations. The specimens were deformed at 1300, 1300 and 1400°C, respectively.

[$\bar{1}$10], (c),(d) [010] and (e),(f) [012] orientations. These specimens were deformed at 1300, 1300 and 1400°C, respectively. Similarly, most dislocations, except for some climbing out from their original slip planes, are observed in the form of trains with traces parallel to ($\bar{1}$12), ($\bar{1}$1$\bar{2}$) and (112) planes for the [$\bar{1}$10], [010] and [012] orientations, respectively. The slip plane that is activated for the [$\bar{1}$10], [010] and [012] orientations is thus determined to be {11$\bar{2}$}. The slip direction on the {11$\bar{2}$} slip plane is considered to be <111> as 1/2<111> is the shortest translation vector on the {11$\bar{2}$} slip plane. This is indeed confirmed by TEM observations of dislocations, as will be described in the next paragraph. These observations clearly indicate that {11$\bar{2}$}<111> is the only slip system that operates in bulk single crystals of Mo_5Si_3.

Fig. 6(a) shows a TEM dislocation structure of a [001]-oriented single crystal deformed at 1300°C. The thin foil was cut parallel to (101). Some dislocations are observed to climb out of their {11$\bar{2}$} slip planes forming nodes here and there. The results of contrast analysis of dislocations made in the framed part of Fig. 6(a) are shown in Fig. 6(b)–(g). Contrast analysis of dislocations was made under weak-beam dark-field conditions, since bright-field imaging of dislocations under two-beam conditions, which is essential to contrast analysis, was found to be very difficult to realize because of the densely populated reciprocal lattice points due to the complex crystal structure of Mo_5Si_3. Dislocations marked A in Fig. 6(b,c,e,f) are invisible when imaged with **g**(reflection vector)=$\bar{3}$30 (Fig. 6(d)) and **g**=2$\bar{3}\bar{1}$ (Fig. 6(g)), so that their Burgers vector (**b**) is determined to be 1/2[$\bar{1}$11]. Dislocations marked B in Fig. 6(b,d,e,g) are
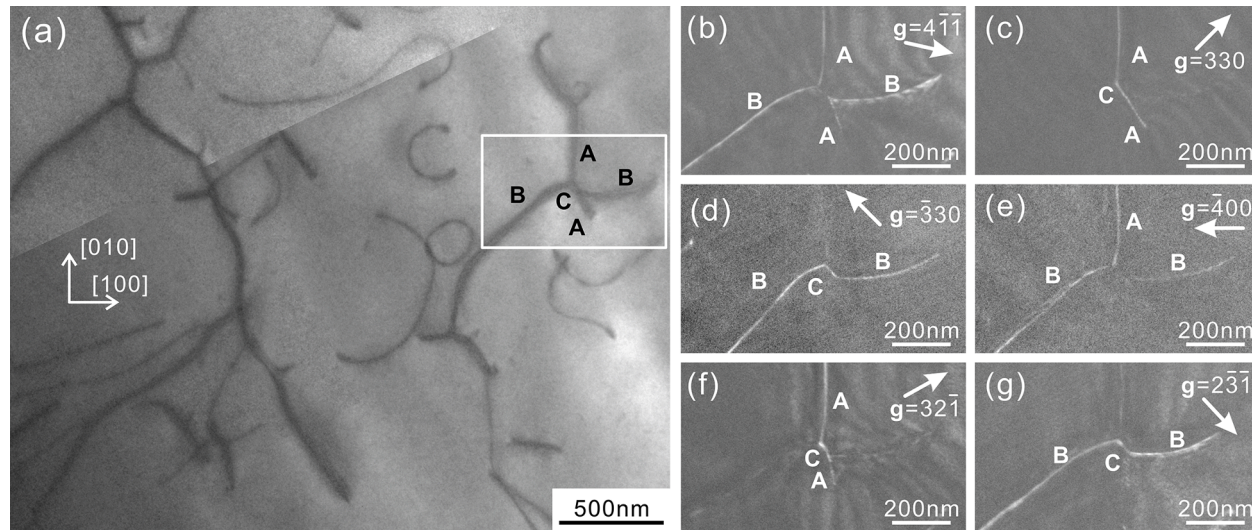
Fig. 6. (a) TEM dislocation structure of a [001]-oriented single crystal deformed at 1300C. Contrast analysis of dislocations in the framed part of (a) are shown in (b)-(g). Reflection vectors (**g**) used are indicated in each of the figures.

invisible when imaged with **g**=330 (Fig. 6(c)) and **g**=32$\bar{1}$ (Fig. 6(f)), so that their Burgers vector (**b**) is 1/2[1$\bar{1}$1]. Dislocations marked C in Fig. 6(c,d,f,g) are, on the other hand, invisible when imaged with **g**=4$\bar{1}\bar{1}$ (Fig. 6(b)) and **g**=$\bar{4}$00 (Fig. 6(e)), so that their Burgers vector (**b**) is [0$\bar{1}$1]. This indicates that dislocations with two different 1/2<111> Burgers vectors originally gliding on their respective {11$\bar{2}$} slip planes climb out of the slip planes and react to form a dislocation node with **b**=[0$\bar{1}$1], according to the following equation,

$$1/2[\bar{1}\bar{1}1] + 1/2[1\bar{1}1] \rightarrow [0\bar{1}1]. \tag{3}$$

Depending on the combination of two different 1/2<111> Burgers vectors, the Burgers vector of the node dislocation can be either [001], <100>, <110> or <011>, according to equations similar to Eq. (3). We speculate that the observation of the dislocation Burgers vector of <110> (Mason and Van Aken, 1995; Yoshimi et al., 2002) and <100> (Meyer et al., 1996) by TEM in single crystals of Mo$_5$Si$_3$ deformed at high temperatures corresponds to such node formation by two different 1/2<111> Burgers vectors of dislocations of the {11$\bar{2}$}<111> slip system that is only the operative slip system in Mo$_5$Si$_3$. Dislocations with **b**=1/2<111> do not dissociate into partial dislocations, as shown in a weak-beam dark-field TEM images of Fig. 6(b)–(g).

3.2. Micropillar single crystals

Typical stress-strain curves obtained in compression at room temperature for micropillar specimens with the [001], [$\bar{1}$10], [010] and [012] orientations are shown in Fig. 7(a). For all the four orientations, failure (as marked with ×) is observed to occur always during elastic loading, regardless of specimen size. Stresses at which failure occurs are very high, exceeding 10 GPa when the specimen size is less than 1 µm. Regardless of crystal orientation, the fracture stress tends to increase with the decrease in specimen size, as shown
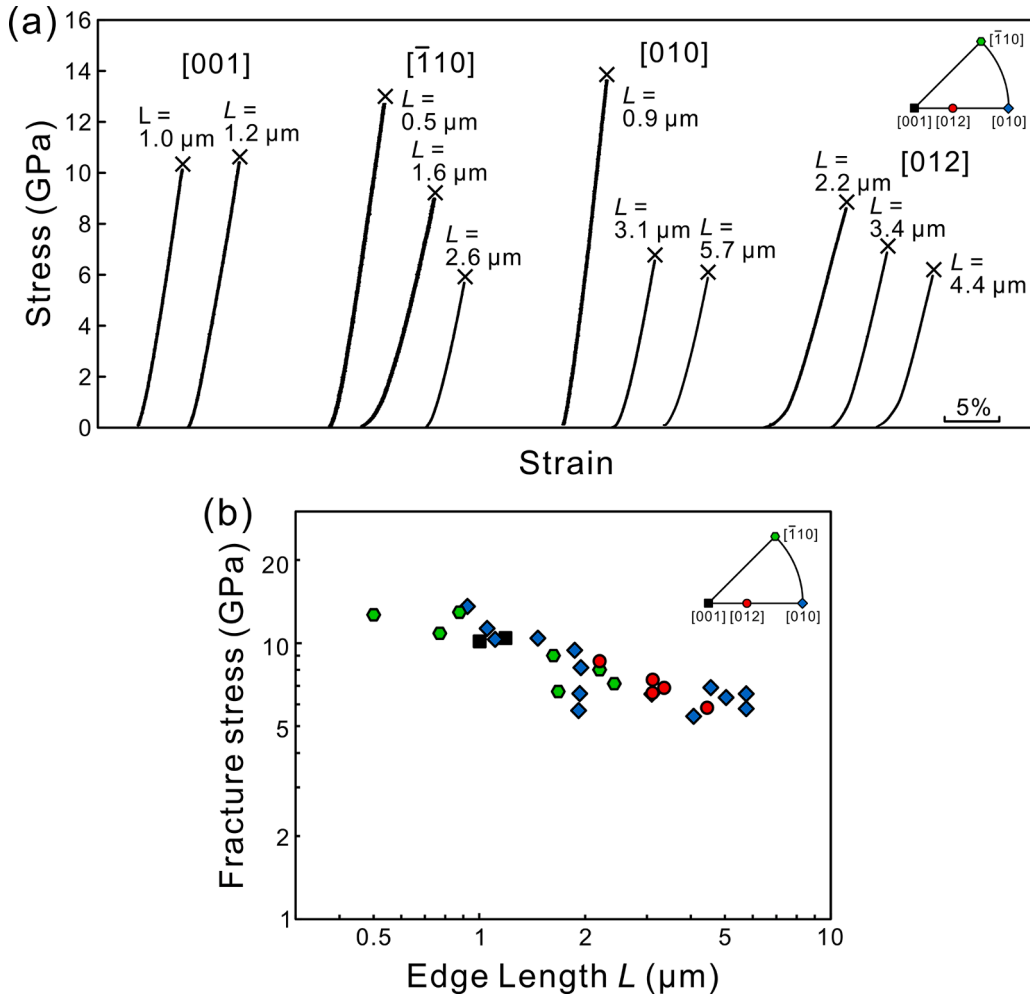

Fig. 7. (a) Typical stress-strain curves obtained in compression at room temperature for micropillar single crystals of Mo$_5$Si$_3$ with [001], [$\bar{1}$10], [010] and [012] orientations. The specimen sizes are indicated in each of the stress-strain curves. Symbols × indicate the occurrence of failure. (b) Specimen size dependence of fracture stress for the four orientations.

in Fig. 7(b). This indicates that unlike in other TM silicides of the TM_5Si_3-types, plastic flow is not possible at room temperature to occur in Mo_5Si_3, even if the specimen size is reduced down to the micron-meter order.

Fig. 8(a)-(d) show SEM images of deformation structures of micropillar specimens with the [001], [$\bar{1}$10], [010] and [012] orientations, respectively. The observations were made along the direction inclined by $30°$ from the loading axis. Catastrophic failure occurs for all specimens without exhibiting any appreciable surface deformation markings. While plastic flow is observed for other TM silicides of the TM_5Si_3-types by micropillar compression testing at room temperature (Kishida et al., 2018, 2020a, 2020b), Mo_5Si_3, is found to be particularly brittle at room temperature.

3.3. Fracture toughness

A load-displacement curve obtained in a single-cantilever bend test for a chevron-notched micro-beam specimen with a notch plane parallel to (001) is depicted in Fig. 9(a). Failure (marked with a symbol ×) occurs in a very brittle manner without any evidence of micro-plasticity in the load-displacement curve. Indeed, the fracture surface is flat, typical of cleavage fracture as shown in Fig. 9(b). The value of fracture toughness calculated with Eqs. (1) and (2) with the maximum load of 0.866 mN is 1.54 MPa•m$^{1/2}$, which is comparable to those (1.79 and 2.43 MPa•m$^{1/2}$) we obtained for Nb_5Si_3 (Kishida et al., 2020b) and Mo_5SiB_2 (Kishida et al., 2018), respectively, but higher than those (0.45–0.73 MPa•m$^{1/2}$) we obtained for Ti_5Si_3 (Kishida et al., 2020a).

4. Discussion

4.1. Operative slip system and the CRSS values

In the present study, ECC imaging in the SEM is proved to be very powerful to identify the operative slip system in bulk Mo_5Si_3 single crystals, for which optical slip trace determination is very difficult to make as plastic flow is observed only at high temperatures where surface oxide films are formed extensively. The slip system of {11$\bar{2}$}<111> is identified to be only the slip system that operates at high temperatures above $1200°C$ in bulk crystals, regardless of crystal orientation. This slip system was also observed by Matsunoshita et al. for a [001]-oriented Mo_5Si_3 grain in a directionally-solidified $MoSi_2$/Mo_5Si_3 eutectic composite deformed in compression at $1000°C$ (Matsunoshita et al., 2016). However, any other predicted (such as (001)<110>, {100}<010> and {110}[001] slip Mason and Van Aken, 1995, and {100}[001] and {110}[001] slip Chu et al., 1999b) and experimentally-identified (such as (001)<110> Mason and Van Aken, 1995; Yoshimi et al., 2002, (001)<100> Meyer et al., 1996 and {100}[001] slip Ochiai et al., 2011) slip systems were never observed to operate for any orientations of bulk single crystals. We have indeed noticed some ambiguity in the slip system identification in these previous studies. As the specimen surface is heavily covered by oxide scale, slip trace determination for the slip plane is very difficult to make. This is well described by Yoshimi et al. who reported that complicated combinations of (001), {100} and {110} slip contribute to deformation of [100] and [101]-oriented crystals (Yoshimi et al., 2002). Mason and Van Aken (1995), on the other hand, assumed that the Burgers vector of the dislocation observed by TEM coincides with the slip direction and inferred the slip
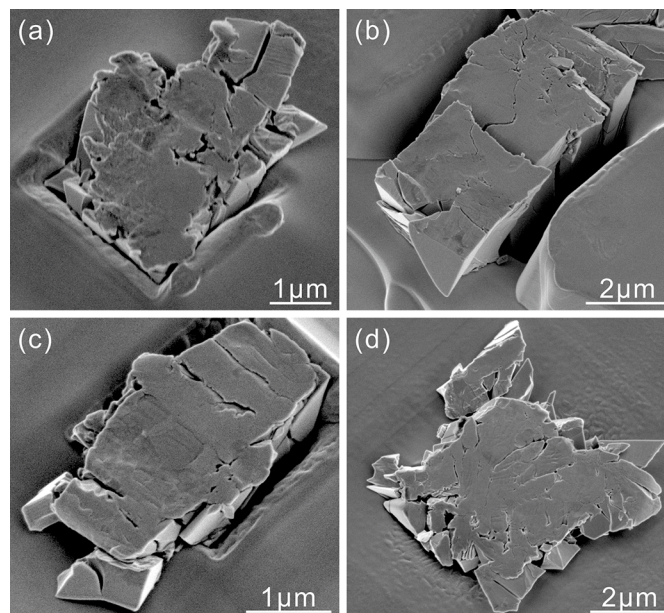

Fig. 8. SEM secondary electron images of fractured micropillar single crystals of Mo_5Si_3 with (a) [001], (b) [$\bar{1}$10], (c) [010] and (d) [012] orientations.
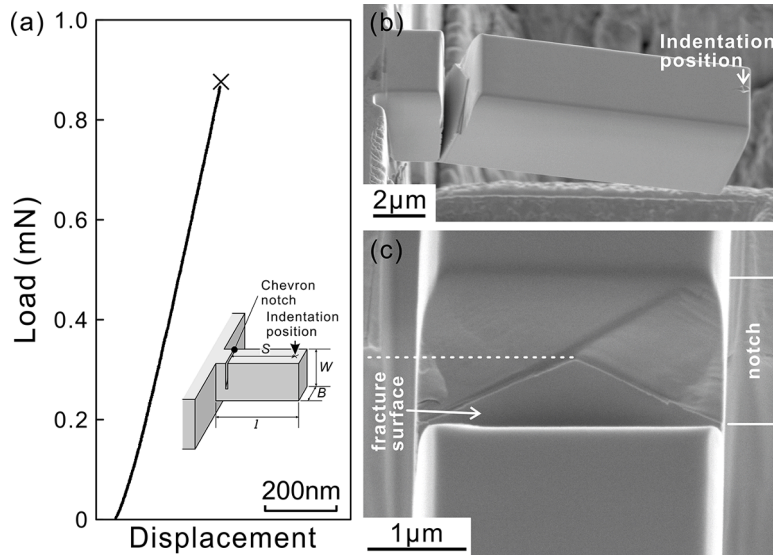
Fig. 9. (a) Load-displacement curve obtained in a single-cantilever bend test for a chevron-notched micro-beam specimen with a notch plane parallel to (001) and (b),(c) SEM secondary electron images of the fractured specimen.

plane for the observed slip direction (parallel to the dislocation Burgers vector) so as to be consistent with their slip system prediction (Meyer et al., 1996). However, due to the very high temperatures during deformation, dislocation climb occurs extensively so that some <100>, <001>, <011> and <110> dislocations are generated as nodes formed by reactions between two different 1/2<111> dislocations (Fig. 6). On top of that, we suspect that TEM Burgers vector determination by Mason and Van Aken (1995), and Yoshimi et al. (2002), is ambiguous as they made contrast analysis under bright-field imaging conditions, under which a two-beam condition is difficult to realize (Meyer et al., 1996). We thus strongly believe that the slip systems previously predicted and experimentally identified do actually not operate in Mo_5Si_3.

We calculated the CRSS values for $\{11\bar{2}\}<111>$ slip with the use of the yield stress values (Fig. 3) and the corresponding Schmid factors (Table 1) in Fig. 10(a) as a function of temperature for each of the four orientations. Although the scatter is rather large, the CRSS value does not vary with orientation at a given temperature, indicating the insensitivity of CRSS for $\{11\bar{2}\}<111>$ slip to crystal orientation.

For various hard and brittle materials, the strain rate $\dot{\gamma}$ can be correlated generally with CRSS τ_c and temperature T by the following equation of $\dot{\gamma} \propto \tau_c^m \exp(-Q/kT)$, where m is the stress exponent, Q is the stress independent activation energy and k is the Boltzmann constant (Fujita et al., 1987). Fig. 10(b) plots logarithms of CRSS for $\{11\bar{2}\}<111>$ slip in bulk single crystals of Mo_5Si_3 as a function of
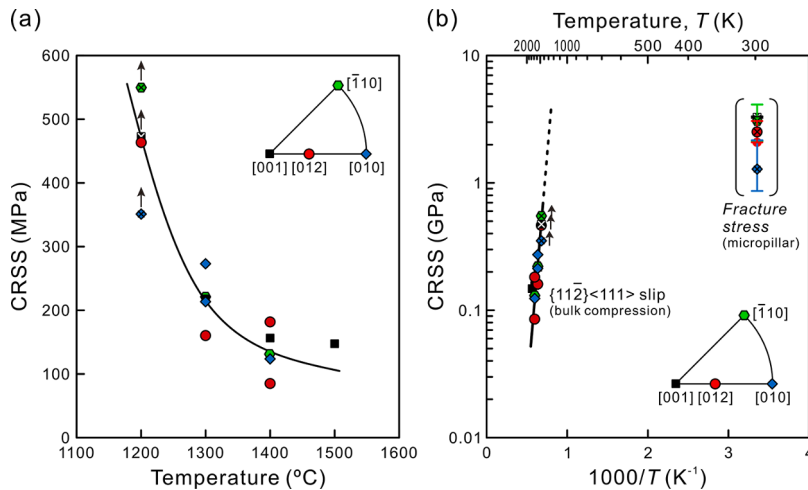

Fig. 10. (a) Temperature dependence of CRSS for $\{11\bar{2}\}<111>$ slip in Mo_5Si_3. (b) Logarithmic plot of CRSS for $\{11\bar{2}\}<111>$ slip in bulk single crystals of Mo_5Si_3 and fracture stresses obtained at room temperature for micropillar single crystals of Mo_5Si_3 plotted as a function of inverse temperature.

inverse temperature $(1/T)$. A linear relationship between $\ln(\tau_c)$ and $(1/T)$ is observed clearly in Fig. 10(b), which indicates that the thermal activation process for $\{11\bar{2}\}$<111> slip in bulk single crystals does not change with temperature at least above 1200°C under constant strain rate deformation. Uniaxial fracture stress values (5.4–13.6 GPa, plotted in Fig. 7(b)) multiplied by the corresponding maximum Schmid factor for $\{11\bar{2}\}$<111> slip are also plotted in Fig. 10(b) as fracture stresses for the ease of comparison with bulk CRSS for $\{11\bar{2}\}$<111> slip. The room-temperature fracture stresses of about 0.9–4.1 GPa are found to be considerably lower than the extrapolated CRSS value for $\{11\bar{2}\}$<111> slip at room temperature deduced from the temperature dependence of CRSS obtained for bulk crystals. The CRSS value for $\{11\bar{2}\}$<111> slip at room temperature could be reduced if some different estimation methods are employed, but we expect that the extrapolated CRSS value could be still very high. The room-temperature brittleness of Mo_5Si_3 is thus due in principle to the difficulty in dislocation motion arising from the very high CRSS value. Brittleness of Mo_5Si_3 at ambient temperature is generally believed to arise from extensive microcracking during processing due to the significantly anisotropic thermal expansion (Chu et al., 1999a, 1999b; Rawn et al., 2005). This may be definitely true for bulk crystals but may not be the case for specimen dimensions of the micrometer order when judged from these very high fracture stresses. According to the model of premature fracture of brittle materials in uniaxial compression proposed by Ashby and co-workers, the critical axial stress σ_c for crack propagation from pre-existing flaws parallel to the compression axis direction is approximated to be $CK_{IC}/(\pi a)^{1/2}$, where a is a size of a pre-existing flaw and C is a constant of the order of unity, depending on material, geometrical configuration and the number density of pre-existing flaws (Ashby and Hallam, 1986; Ashby and Sammis, 1990; Sammis and Ashby, 1986). With $C = 1$, $K_{IC} = 1.54$ MPa•m$^{1/2}$ and $\sigma_c = 5.4$-13.6 GPa, a critical flaw size is estimated to be 4-26 nm. Fabrication of micropillar specimens would be possible avoiding the incorporation of microcracks of the above size.

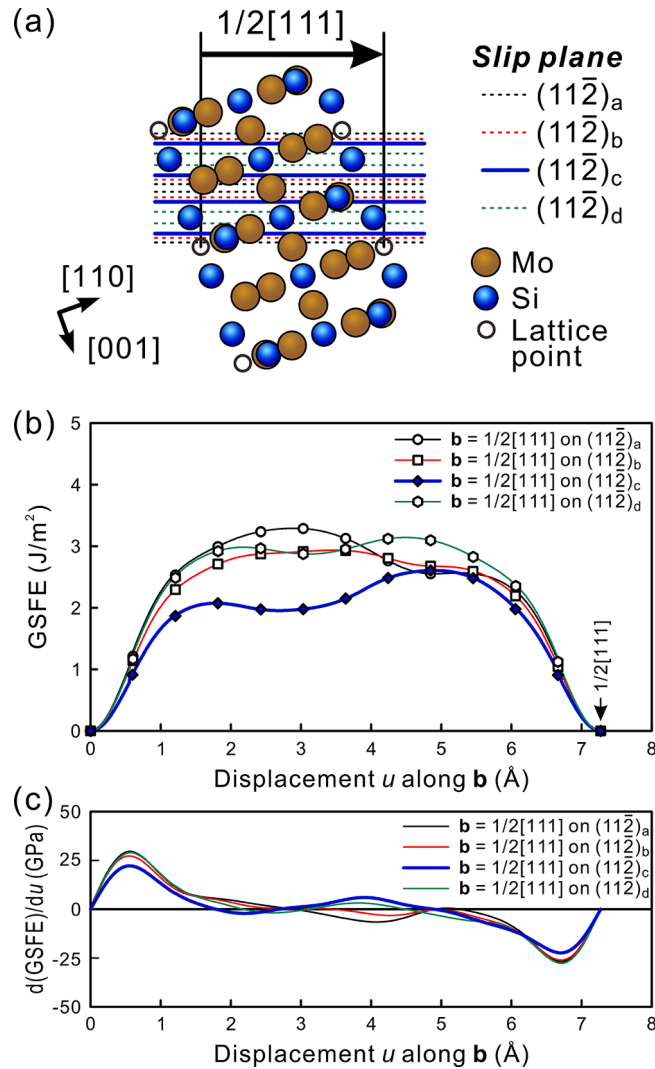**Fig. 11.** (a) Four crystallographically non-equivalent slip planes considered for slip on $\{11\bar{2}\}$<111>. (b) Calculated GSFE curves and (c) their derivatives (corresponding to the gradient of the GSFE curve) as a function of displacement u along their slip directions for $\{11\bar{2}\}$<111> in Mo_5Si_3.

4.2. Selection of {112} slip plane and slip system

We made GSFE calculations for the $\{11\overline{2}\}<111>$ slip system in Mo_5Si_3, in order to precisely identify the $\{11\overline{2}\}$ slip plane where dislocations move and to see any possibility for dissociation of the $1/2<111>$ dislocation on the slip plane. There are four crystallographically non-equivalent $\{11\overline{2}\}$ slip planes to be considered as illustrated in Fig. 11(a) as $(11\overline{2})_a$ to $(11\overline{2})_d$, respectively. The calculation was made for displacements along the slip direction on the relevant slip plane, as no dislocation dissociation was observed for the $1/2<111>$ dislocation gliding on the $\{11\overline{2}\}$ slip plane (Fig. 6(f)). The GSFE curves and their derivatives (corresponding to the gradient of the GSFE curve) for the $\{11\overline{2}\}<111>$ slip system are plotted in Fig. 11(b) and (c) as a function of displacement u along the $<111>$ slip direction, respectively. The unstable stacking fault energy (the maximum of GSFE curve), stable stacking fault energy and the maximum value of the derivative curve (corresponding to the lattice resistance against slip deformation, i.e., theoretical shear strength τ_{th}) are summarized in Table 2. For $\{11\overline{2}\}<111>$ slip, both the unstable stacking fault energy and the maximum of the derivative curve are the lowest on $(11\overline{2})_c$, indicating that the $(11\overline{2})_c$ plane is preferred as the glide plane for the $1/2<111>$ dislocation from the energetically view point. Although there exists an energy minimum of $1.98 J/m^2$ in the GSFE curve along $<111>$, the energy minimum is too shallow to allow the $1/2<111>$ dislocation to dissociate into two partial dislocations on the $(11\overline{2})_c$ plane. This is consistent with the TEM result in the present study (Fig. 6(f)).

4.3. Kinks formed as deformation bands

In our previous study, we have reported the formation of two types of deformation bands; $\{\overline{2}118\}$ deformation twins and kink bands parallel to (0001) in $[2\overline{11}24]$-oriented bulk single crystals of Ti_5Si_3 with the hexagonal $D8_8$ structure deformed in compression at high temperatures above 1300°C (Kishida et al., 2010). Similar deformation bands are found to form in Mo_5Si_3 single crystals of Mo_5Si_3 deformed at high temperatures. Here, we discuss details of deformation bands formed in Mo_5Si_3 by compression at 1300°C. Fig. 12(a) and (b) show deformation bands observed on two orthogonal side surfaces of a $[\overline{1}10]$-oriented bulk single crystal. Trace analysis conducted on the two side faces reveals that the deformation bands are inclined by about 20° (nearly parallel to $(\overline{44}1)$) – 30° (nearly parallel to $(\overline{55}2)$) from the $(\overline{1}10)$ initial compression plane. Electron backscatter diffraction (EBSD) analysis made on the (110) side surface (the orientation maps showing the surface normal and loading axis directions, respectively in Fig. 12 (c) and (d)) indicates that changes in crystallographic orientation occur gradually within each of deformation bands (but not discretely across the band boundary). The maximum misorientation angle ranges from 2° to 20° depending seemingly on the thickness of the deformation band, as shown in Fig. 12(e) for the case of misorientation with respect to the loading axis direction of Fig. 12(d). When misorientation within deformation bands is inspected with respect to the (110) side surface normal (Fig. 12(c)), on the other hand, no misorientation is noticed for any deformation bands, exhibiting essentially the same crystal orientation as the crystal outside deformation bands. This indicates that the crystal rotation within deformation bands occurs around [110] (i.e., parallel to the (110) side surface normal).

If we assume that these deformation bands are deformation twins, we can deduce the twinning elements as $K_1 = (\overline{88}1)$, $\eta_1 = [1\overline{11}6]$, $K_2 = (001)$ and $\eta_2 = [\overline{1}10]$ with the stereographic analysis (Fig. 12(f)) of the orientation relationship of the matrix and twins with the maximum misorientation of about 20° (marked with an arrow in Fig. 12(d) and (e)). However, it seems difficult to conclude that these deformation bands are deformation twins, as (1) the crystal misorientation occurs only gradually within the deformation band but not discretely across the band boundary, (2) the (maximum) misorientation angle varies from band to band and (3) the $(\overline{88}1)$ K_1 plane does not necessarily coincide with the approximate habit plane of $(\overline{44}1)$. It seems more reasonable to conclude that these deformation bands are kink bands according to the reasons described below. Kink bands are known to form when a crystal having only one operative slip system is uniaxially compressed along a direction (nearly) perpendicular to the slip plane normal with edge dislocations being aligned perpendicular to the slip plane (Frank and Stroh, 1952; Gong et al., 2018; Hagihara et al., 2016; Hess and Barrett, 1949; Higashi et al., 2018; Paul et al., 2021). In Mo_5Si_3, $\{11\overline{2}\}<111>$ slip is only the operative slip system, and $(\overline{1}12)[\overline{1}1\overline{1}]$ slip is identified to operate in $[\overline{1}10]$-oriented bulk single crystals, as described in Section 3.1.2. The angle between the $[\overline{1}10]$ loading axis and the normal of the $(\overline{1}12)$ slip plane is as large as about 70°. In that circumstance, kink bands are considered to form by the accumulation of $1/2[\overline{1}1\overline{1}]$ edge dislocations in the wall perpendicular to the $(\overline{1}12)$ slip plane (Fig. 12(g)). Then, [110] is expected to the rotation axis of the crystal orientation within the deformation band, and the kink boundary plane that is perpendicular both to the $(\overline{1}12)$ slip plane and to the

Table 2

Summary of first-principles DFT calculations of generalized stacking fault energy (GSFE) for $\{11\overline{2}\}<111>$ slip in Mo_5Si_3.

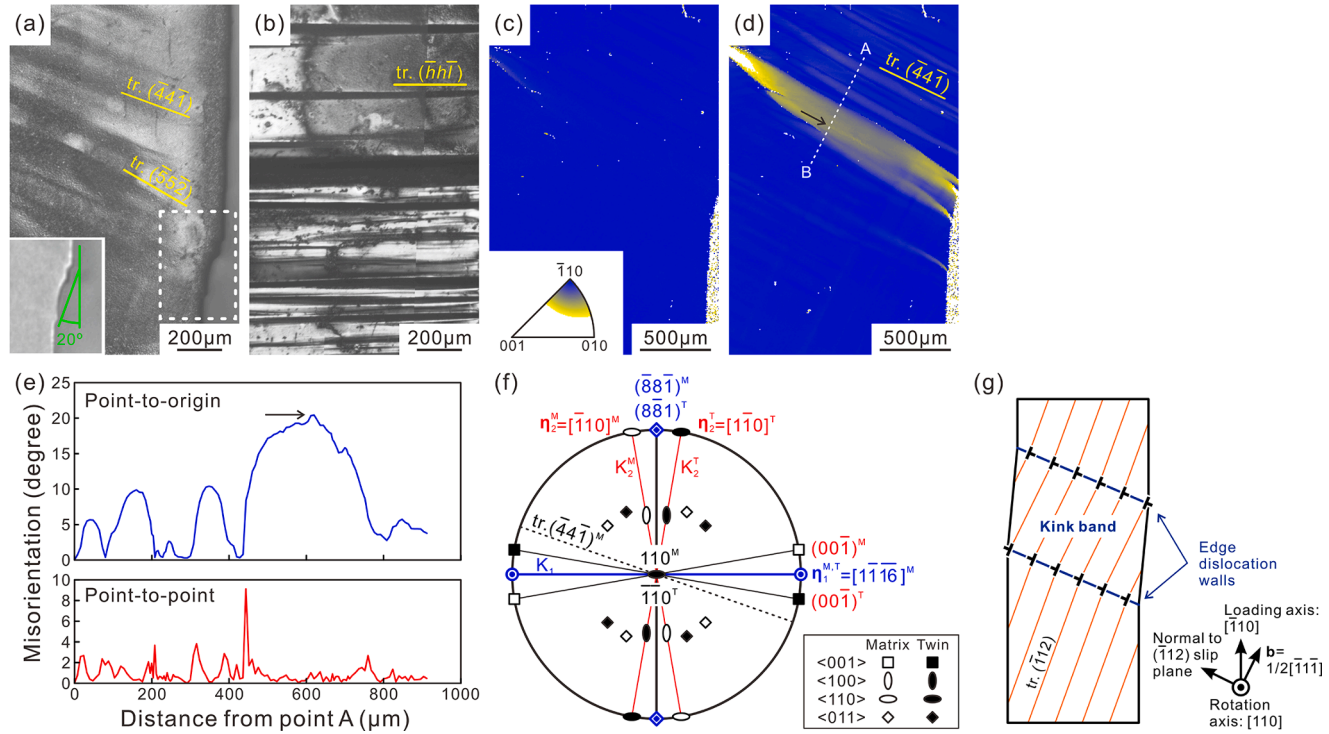| Slip plane	Slip direction	Unstable stacking fault energy (J/m²)	Ideal shear strength, τ_{th} (GPa)
$\{11\overline{2}\}_a$	$<111>$	3.29	29.7
	$<\overline{111}>$	3.29	26.9
$\{11\overline{2}\}_b$	$<111>$	2.94	27.3
	$<\overline{111}>$	2.94	26.1
$\{11\overline{2}\}_c$	$<111>$	**2.60**	**22.2**
	$<\overline{111}>$	**2.60**	**22.4**
$\{11\overline{2}\}_d$	$<111>$	3.14	29.0
	$<\overline{111}>$	3.14	27.7

Fig. 12. Deformation bands developed in a $[\bar{1}10]$-oriented single crystal of Mo$_5$Si$_3$ deformed at 1300°C. OM images of two orthogonal surfaces of (a) (110) and (b) (00$\bar{1}$). EBSD orientation maps showing the directions parallel to (c) the (110) surface normal and (d) the loading axis direction. (e) Orientation difference between adjacent analysis points (point-to-point) on the line between A and B in Fig. 12(d) as well as the accumulated values of the orientation difference (point-to-origin). (f) Stereographic projection of the orientation relationship between the regions inside and outside of the deformation band with the approximate habit plane of ($\bar{4}4\bar{1}$). (g) Schematic illustration of a kink band formed by 1/2[$\bar{1}1\bar{1}$] edge dislocations on ($\bar{1}12$) slip plane.

$[\bar{1}1\bar{1}]$ slip direction is expected to incline by about 70° from the $(\bar{1}10)$ initial compression plane (Fig. 12(g)). All these aspects are indeed actually observed experimentally in $[\bar{1}10]$-oriented bulk single crystals deformed at 1300°C (Fig. 12). The spacing of $1/2[\bar{1}1\bar{1}]$ edge dislocations in the kink wall perpendicular to the $(\bar{1}12)$ slip plane is estimated to be 4 and 2 nm for the tilt angle of 10 and 20°, respectively. Deformation bands observed in $[2\bar{1}\bar{1}24]$-oriented bulk single crystals of Ti_5Si_3 deformed in compression at 1300°C (Kishida et al., 2010) are also considered as kink bands formed by [0001] edge dislocations accumulated in the wall perpendicular to the $\{1\bar{1}00\}$ prism slip plane. In Mo_5Si_3, the [100] orientation also satisfies the geometrical requirement for kink band formation as the $[\bar{1}10]$ orientation does. Yet, kink band formation was not observed for the [100] orientation. More study is needed to clarify the formation condition of kink bands in Mo_5Si_3.

5. Conclusions

The plastic deformation behavior of single crystals of Mo_5Si_3 with the tetragonal $D8_m$ structure has been investigated in compression as a function of crystal orientation and temperature (1200–1500°C) in the bulk form and as a function of crystal orientation and specimen size at room temperature in the micropillar form. The results obtained are summarized as follows.

(1) Plastic flow is observed only at high temperatures above 1200°C in bulk single crystals of Mo_5Si_3, but any plastic flow is not detected at room temperature when small single crystals of the micron-meter size are tested in compression.
(2) The slip system of $\{11\bar{2}\}\langle111\rangle$ is identified to be the only slip system that operates at high temperatures. The CRSS for $\{11\bar{2}\}\langle111\rangle$ slip decreases rapidly with increasing temperature, suggesting the existence of a high Peierls stress.
(3) Indeed, the CRSS for $\{11\bar{2}\}\langle111\rangle$ slip at room temperature estimated from the extrapolation of the temperature dependence of CRSS obtained for bulk crystals is considerably higher than fracture stresses obtained for micropillar crystals, indicating that the room-temperature brittleness is due in principle to the difficulty in dislocation motion arising from the very high CRSS value.
(4) The value of fracture toughness evaluated with a chevron-notched micro-beam specimen with a notch plane parallel to (001) is 1.54 MPa•m$^{1/2}$, which is comparable to those reported for other transition-metal (TM) silicides of the TM_5Si_3-type.

CRediT authorship contribution statement

Kyosuke Kishida: Investigation, Data curation, Visualization, Writing – original draft, Writing – review & editing, Funding acquisition. **Zhenghao Chen:** Investigation, Visualization. **Hirotaka Matsunoshita:** Investigation, Writing – original draft. **Takuto Maruyama:** Investigation, Writing – original draft. **Takayoshi Fukuyama:** Investigation. **Yuta Sasai:** Investigation. **Haruyuki Inui:** Supervision, Conceptualization, Methodology, Funding acquisition, Writing – original draft, Writing – review & editing. **Martin Heilmaier:** Supervision, Writing – review & editing.

Declaration of Competing Interest

The authors declare that they have no known competing financial interests or personal relationships that could have appeared to influence the work reported in this paper.

Acknowledgments

References

Akinc, M., Meyer, M.K., Kramer, M.J., Thom, A.J., Huebsch, J.J., Cook, B., 1999. Boron-doped molybdenum silicides for structural applications. Mater. Sci. Eng. A 261, 16–23.

Ashby, M., Sammis, C., 1990. The damage mechanics of brittle solids in compression. Pure Appl. Geophys. 133, 489–521.

Ashby, M.F., Hallam, S.D., 1986. The failure of brittle solids containing small cracks under compressive stress states. Acta Metall. 34, 497–510.

Azim, M.A., Christ, H.J., Gorr, B., Kowald, T., Lenchuk, O., Albe, K., Heilmaier, M., 2017. Effect of Ti addition on the thermal expansion anisotropy of Mo_5Si_3. Acta Mater. 132, 25–34.

Bewlay, B.P., Jackson, M.R., Subramanian, P.R., Zhao, J.C., 2003. A review of very-high-temperature Nb-silicide-based composites. Metall. Mater. Trans. A 34, 2043–2052.

Chen, H., Ma, Q., Shao, X., Ma, J., Wnag, C., Huang, B., 2014. Microstructure, mechanical properties and oxidation resistance of Mo_5Si_3-Al_2O_3 composite. Mater. Sci. Eng. A 592, 12–18.

Chen, Z., Paul, B., Majumdar, S., Okamoto, N.L., Kishida, K., Inui, H., Otani, S., 2021. Room-temperature deformation of single crystals of ZrB_2 and TiB_2 with the hexagonal AlB_2 structure investigated by micropillar compression. Sci. Rep. 11, 14265.

Christensen, A.N., 1983. Preparation and characterization of Mo_3Si and Mo_5Si_3. Acta Chem. Scanda. A 37, 519–522.

Chu, F., Thoma, D., McClellan, K., Peralta, P., 1999a. Mo_5Si_3 single crystals: physical properties and mechanical behavior. Mater. Sci. Eng. A 261, 44–52.

Chu, F., Thoma, D., McClellan, K., Peralta, P., He, Y., 1999b. Synthesis and properties of Mo_5Si_3 single crystals. Intermetallics 7, 611–620.

Dharmawardhana, C.C., Sakidja, R., Aryal, S., Ching, W.Y., 2015. In search of zero thermal expansion anisotropy in Mo_5Si_3 by strategic alloying. J. Alloy. Compd. 620, 427–433.

Deng, X., Bitler, J., Chawla, K.K., Patterson, B.R., 2010. Toughness measurement of cemented carbides with chevron-notched three-point bend test. Adv. Eng. Mater. 12, 948–952.

Frank, F., Stroh, A., 1952. On the theory of kinking. Proc. Phys. Soc. B 65, 811–821.

Fujita, S., Maeda, K., Hyodo, S., 1987. Dislocation glide in 6H SiC single crystals subjected to high-temperature deformation. Philos. Mag. A 55, 203–215.

Fujiwara, K., Matsunoshita, H., Sasai, Y., Kishida, K., Inui, H., 2014. Effects of ternary additions on the microstructure and thermal stability of directionally-solidified $MoSi_2/Mo_5Si_3$ eutectic composites. Intermetallics 52, 72–85.

Gong, W., Aizawa, K., Harjo, S., Zheng, R., Kawasaki, T., Abe, J., Kamiyama, T., Tsuji, N., 2018. Deformation behavior of as-cast and as-extruded $Mg_{97}Zn_1Y_2$ alloys during compression as tracked by *in situ* neutron diffraction. Int. J. Plast. 111, 288–306.

Gutierrez-Urrutia, I., Zaefferer, S., Raabe, D., 2009. Electron channeling contrast imaging of twins and dislocations in twinning-induced plasticity steels under controlled diffraction conditions in a scanning electron microscope. Scr. Mater. 61, 737–740.

Hagihara, K., Mayama, T., Honnami, M., Yamasaki, M., Izuno, H., Okamoto, T., Ohashi, T., Nakano, T., Kawamura, Y., 2016. Orientation dependence of the deformation kink band formation behavior in Zn single crystal. Int. J. Plast. 77, 174–191.

Han, S., Crimp, M.A., 2020. ECCI analysis of shear accommodations at grain boundaries in commercially pure alpha titanium. Int. J. Plastic. 131, 102731.

Hashizume, Y., Inomoto, M., Okamoto, N.L., Inui, H., 2021. Plastic deformation of single crystals of the δ_{1p} and δ_{1k} intermetallic compounds in the Fe–Zn System by micropillar compression. Int. J. Plastic. 136, 102889.

Hashizume, Y., Inomoto, M., Okamoto, N.L., Takebayashi, H., Inui, H., 2020. Micropillar compression deformation of single crystals of the intermetallic compound Γ-Fe_4Zn_9. Acta Mater. 199, 514–522.

Hess, J.B., Barrett, C.S., 1949. Structure and nature of kink bands in zinc. JOM 1, 599–606.

Higashi, M., Momono, S., Kishida, K., Okamoto, N.L., Inui, H., 2018. Anisotropic plastic deformation of single crystals of the MAX phase compound Ti_3SiC_2 investigated by micropillar compression. Acta Mater. 161, 161–170.

Inui, H., Ishikawa, K., Yamaguchi, M., 2000a. Creep deformation of single crystals of binary and some ternary $MoSi_2$ with the $C11_b$ structure. Intermetallics 8, 1159–1168.

Inui, H., Ishikawa, K., Yamaguchi, M., 2000b. Effects of alloying elements on plastic deformation of single crystals of $MoSi_2$. Intermetallics 8, 1131–1145.

Ito, K., Inui, H., Shirai, Y., Yamaguchi, M., 1995. Plastic deformation of $MoSi_2$ single crystals. Philos. Mag. A 72, 1075–1097.

Ito, K., Yano, T., Nakamoto, T., Inui, H., Yamaguchi, M., 1997. Microstructure and mechanical properties of $MoSi_2$ single crystals and directionally solidified $MoSi_2$-based alloys. Prog. Mater. Sci. 42, 193–207.

Jackson, M., Bewlay, B., Rowe, R., Skelly, D., Lipsitt, H., 1996. High-temperature refractory metal-intermetallic composites. JOM 48, 39–44.

Kishida, K., Fujiwara, M., Adachi, H., Tanaka, K., Inui, H., 2010. Plastic deformation of single crystals of Ti_5Si_3 with the hexagonal $D8_8$ structure. Acta Mater. 58, 846–857.

Kishida, K., Fukuyama, T., Maruyama, T., Inui, H., 2020a. Room temperature deformation of single crystals of Ti_5Si_3 with the hexagonal $D8_8$ structure investigated by micropillar compression tests. Sci. Rep. 10, 17983.

Kishida, K., Maruyama, T., Fukuyama, T., Inui, H., 2020b. Micropillar compression deformation of single crystals of α-Nb_5Si_3 with the tetragonal $D8_l$ structure. Sci. Tech. Adv. Mater. 21, 805–816.

Kishida, K., Maruyama, T., Matsunoshita, H., Fukuyama, T., Inui, H., 2018. Micropillar compression deformation of single crystals of Mo_5SiB_2 with the tetragonal $D8_l$ structure. Acta Mater. 159, 416–428.

Kishida, K., Nakatsuka, S., Nose, H., Inui, H., 2022a. Room-temperature deformation of single crystals of transition-metal disilicides ($TMSi_2$) with the $C11_b$ (TM= Mo) and C40 (TM= V, Cr, Nb and Ta) structures investigated by micropillar compression. Acta Mater. 223, 117468.

Kishida, K., Okutani, M., Inui, H., 2022b. Direct observation of zonal dislocation in complex materials by atomic-resolution scanning transmission electron microscopy. Acta Mater. 228, 117756.

Kishida, K., Shinkai, Y., Inui, H., 2020c. Room temperature deformation of 6H–SiC single crystals investigated by micropillar compression. Acta Mater. 187, 19–28.

Kresse, G., Furthmüller, J., 1996. Efficient iterative schemes for ab initio total-energy calculations using a plane-wave basis set. Phys. Rev. B 54, 11169–11186.

Maloy, S.A., Mitchell, T.E., Heuer, A.H., 1995. High temperature plastic anisotropy in $MoSi_2$ single crystals. Acta metall. Mater. 43, 657–668.

Mason, D.P., Van Aken, D.C., 1995. On the creep of directionally solidified $MoSi_2$-Mo_5Si_3 eutectics. Acta Metall. Mater. 43, 1201–1210.

Matsunoshita, H., Sasai, Y., Fujiwara, K., Kishida, K., Inui, H., 2016. Plastic deformation of directionally solidified ingots of binary and some ternary $MoSi_2/Mo_5Si_3$ eutectic composites. Sci. Tech. Adv. Mater. 17, 517–529.

Meyer, M.K., Kramer, M.J., Akinca, M., 1996. Compressive creep behavior of Mo_5Si_3 with the addition of boron. Intermetallics 4, 273–281.

Mitra, R., 2006. Mechanical behaviour and oxidation resistance of structural silicides. Int. Mater. Rev. 51, 13–64.

Mitra, R., 2015. Structural Intermetallics and Intermetallic Matrix Composites. CRC press, Boca Raton.

Monkhorst, H.J., Pack, J.D., 1976. Special points for Brillouin-zone integrations. Phys. Rev. B 13, 5188–5192.

Mueller, M., Pejchal, V., Žagar, G., Singh, A., Cantoni, M., Mortensen, A., 2015. Fracture toughness testing of nanocrystalline alumina and fused quartz using chevron-notched microbeams. Acta Mater. 86, 385–395.

Obert, S., Kauffmann, A., Heilmaier, M., 2020. Characterisation of the oxidation and creep behaviour of novel Mo-Si-Ti alloys. Acta Mater. 184, 132–142.

Obert, S., Kauffmann, A., Pretzler, R., Schliephake, D., Hinrichs, F., Heilmaier, M., 2021. The creep and oxidation behaviour of pesting-resistant $(Mo,Ti)_5Si_3$-containing eutectic-eutectoid Mo-Si-Ti alloys. Metals 11, 169.

Ochiai, Y., Kishida, K., Tanaka, K., Inui, H., 2011. Mechanical properties of Cr_5Si_3 with the $D8_m$ structure. MRS Proc. 1295, 213–218.

Okamoto, N.L., Inomoto, M., Adachi, H., Takebayashi, H., Inui, H., 2014. Micropillar compression deformation of single crystals of the intermetallic compound ζ-$FeZn_{13}$. Acta Mater. 65, 229–239.

Paul, B., Okamoto, N.L., Kusakari, M., Chen, Z., Kishida, K., Inui, H., Otani, S., 2021. Plastic deformation of single crystals of CrB_2, TiB_2 and ZrB_2 with the hexagonal AlB_2 structure. Acta Mater. 211, 116857.

Perdew, J.P., Burke, K., Ernzerhof, M., 1996. Generalized gradient approximation made simple. Phys. Rev. Lett. 77, 3865–3868.

Perepezko, J.H., 2009. The hotter the engine, the better. Science 326, 1068–1069.

Perepezko, J.H., Kruger, M., Heilmaier, M., 2021. Mo-silicide alloys for high-temperature structural applications. Mater. Perform. Charact. 10, 122–145.

Petrovic, J.J., Vasudevan, A.K., 1999. Key developments in high temperature structural silicides. Mater. Sci. Eng. A 261, 1–5.

Picard, Y.N., Liu, M., Lammatao, J., Kamaladasa, R., De Graef, M., 2014. Theory of dynamical electron channeling contrast images of near-surface crystal defects. In: Ultramicroscopy, 146, pp. 71–78.

Rawn, C.J., Schneibel, J.H., Fu, C.L., 2005. Thermal expansion anisotropy and site occupation of the pseudo-binary molybdenum vanadium silicide Mo_5Si_3-V_5Si_3. Acta Mater. 53, 2431–2437.

Sammis, C., Ashby, M., 1986. The failure of brittle porous solids under compressive stress states. Acta Metall. 34, 511–526.

Simkin, B., Crimp, M., 1999. An experimentally convenient configuration for electron channeling contrast imaging. Ultramicroscopy 77, 65–75.

Tsakiropoulos, P., 2018. On Nb silicide based alloys: alloy design and selection. Materials 11, 844.

Tsakiropoulos, P., 2022. Alloys for application at ultra-high temperatures: Nb-silicide *in situ* composites challenges, breakthroughs and opportunities. Prog. Mater. Sci. 123, 100714.

Vega Farje, J.A., Matsunoshita, H., Kishida, K., Inui, H., 2019. Microstructure and mechanical properties of a $MoSi_2$-Mo_5Si_3 eutectic composite processed by laser surface melting. Mater. Charact. 148, 162–170.

Villars, P., Calvert, L.D., 1985. Pearson's Handbook of Crystallographic Data for Intermetallic Phases, 2. American Society for Metals, Metals Park.

Vitek, V., Paidar, V., Hirth, J.P., 2008. Non-planar dislocation cores: a ubiquitous phenomenon affecting mechanical properties of crystalline materials. In: Dislocations in Solids, 14. Elsevier, Amsterdam, pp. 439–514.

Weidner, A., Biermann, H., 2015. Case studies on the application of high-resolution electron channelling contrast imaging–investigation of defects and defect arrangements in metallic materials. Philos. Mag. 95, 759–793.

Wilkinson, A.J., Hirsch, P.B., 1997. Electron diffraction based techniques in scanning electron microscopy of bulk materials. Micron 28, 279–308.

Yamaguchi, M., Inui, H., Ito, K., 2000. High-temperature structural intermetallics. Acta Mater. 48, 307–322.

Yeh, C.L., Peng, J.A., 2017. Effects of oxide precursors and fabrication of Mo_5Si_3-Al_2O_3 composites via thermite-based combustion synthesis. Intermetallics 83, 87–91.

Yoshimi, K., Yoo, M.H., Wereszczak, A.A., Borowicz, S.M., George, E.P., Miura, E., Hanada, S., 2002. Deformation behavior of Mo_5Si_3 single crystal at high temperatures. Mater. Sci. Eng. A 329, 228–234.

Yuge, K., 2017. First-principles study on segregation of ternary additions for $MoSi_2$/Mo_5Si_3 interface. Calphad 56, 150–153.

Zaefferer, S., Elhami, N.N., 2014. Theory and application of electron channelling contrast imaging under controlled diffraction conditions. Acta Mater. 75, 20–50.

Zhao, J.C., Westbrook, J.H., 2003. Ultrahigh-temperature materials for jet engines. MRS Bull. 28, 622–630.

Zhu, C., Koizumi, Y., Chiba, A., Yuge, K., Kishida, K., Inui, H., 2020. Pattern formation mechanism of directionally-solidified $MoSi_2$/Mo_5Si_3 eutectic by phase-field simulation. Intermetallics 116, 106590.

Zhu, C., Yamamoto, J., Koizumi, Y., Yuge, K., Kishida, K., Inui, H., 2021. Comprehensive phase field study on directionally-solidified $MoSi_2$/Mo_5Si_3 eutectic alloy. Mater. Sci. Forum 1016, 749–754.